



CHORUS

This is the accepted manuscript made available via CHORUS. The article has been published as:

Bulk Fermi surface of the Weyl type-II semimetallic candidate NbIrTe₄

Rico Schönemann, Yu-Che Chiu, Wenkai Zheng, Victor L. Quito, Shouvik Sur, Gregory T. McCandless, Julia Y. Chan, and Luis Balicas

Phys. Rev. B **99**, 195128 — Published 15 May 2019

DOI: [10.1103/PhysRevB.99.195128](https://doi.org/10.1103/PhysRevB.99.195128)

Bulk Fermi surface of the Weyl type-II semimetallic candidate NbIrTe₄

Rico Schönemann,^{1,*} Yu-Che Chiu,^{1,2} Wenkai Zheng,¹ Victor L. Quito,³
Shouvik Sur,^{4,2} Gregory T. McCandless,⁵ Julia Y. Chan,⁵ and Luis Balicas^{1,†}

¹*National High Magnetic Field Laboratory, Florida State University, Tallahassee, Florida 32306, USA*

²*Department of Physics, Florida State University, Tallahassee, Florida 32306, USA*

³*Iowa State University, Department of Physics and Astronomy, Ames, Iowa 50011, USA*

⁴*Northwestern University, Evanston, Illinois 60208, USA*

⁵*The University of Texas at Dallas, Department of Chemistry and Biochemistry, Richardson, Texas 75080 USA*

(Dated: April 30, 2019)

Recently, a new group of layered transition-metal tetra-chalcogenides was proposed via first principles calculations to correspond to a new family of Weyl type-II semimetals with promising topological properties in the bulk as well as in the monolayer limit. In this article, we present measurements of the Shubnikov-de Haas (SdH) and de Haas-van Alphen effects under high magnetic fields for the type-II Weyl semimetallic candidate NbIrTe₄. We find that the angular dependence of the observed Fermi surface extremal cross-sectional areas agree well with our DFT calculations supporting the existence of Weyl type-II points in this material. Although we observe a large and non-saturating magnetoresistivity in NbIrTe₄ under fields all the way up to 35 T, Hall-effect measurements indicate that NbIrTe₄ is not a compensated semimetal. The transverse magnetoresistivity displays a four-fold angular dependence akin to the so-called butterfly magnetoresistivity observed in nodal line semimetals. We conclude that the field and this unconventional angular-dependence are governed by the topography of the Fermi-surface and the resulting anisotropy in effective masses and in carrier mobilities.

I. INTRODUCTION

Recently, Weyl fermions have emerged as a heavily studied subject combining key concepts from high energy and condensed matter physics¹. In a Weyl semimetal, Weyl fermions emerge around the touching points between linearly dispersing valence and conduction bands. Type-I Weyl points correspond to the “conventional” Weyl Fermions of quantum field theory. Weyl semimetals require broken inversion or time reversal symmetry for the Weyl nodes of opposite chirality to separate in k -space or to prevent their pairwise annihilation. Insofar, several candidates for type-I Weyl semimetals have been found, most notably the compounds belonging to the TaAs family²⁻⁵. In these compounds angle resolved photoemission spectroscopy (ARPES) and magneto transport experiments were able to reveal a few characteristic signatures of Weyl semimetals like topological Fermi arcs on their surface, the emergence of a controversial negative longitudinal magnetoresistance (NLMR) when magnetic and electric fields are aligned⁶, and the observation of the so-called Weyl-orbits⁷. exploring the Fermi arcs.

Weyl type-II fermions are predicted to emerge at the boundary between hole- and electron-pockets resulting from strongly tilted Weyl cones that break Lorentz invariance within the crystal and, therefore, have no equivalents in high energy physics⁸. Candidates for Weyl type-II semimetals include non-centrosymmetric materials whose inversion symmetry is broken like the layered orthorhombic transition-metal dichalcogenides MoTe₂ and WTe₂^{9,10}, as well as MoP₂ and WP₂¹¹ which do not crystallize in a layered structure. However, type-II Weyl points have been predicted to emerge in the ternary tellurides TaIrTe₄ and NbIrTe₄^{12,13}. In fact, the entire fam-

ily of the $MM'Te_4$, where $M = \text{Ta}$ or Nb and $M' = \text{Ir}$ or Rh , is candidate for bulk Weyl type-II semimetallic states and is also predicted to display a topological quantum spin hall insulating phase in the monolayer limit¹⁴. TaIrTe₄ was the first representative within this family of materials to be claimed to exhibit a Weyl semimetallic state¹². It was shown that by including spin-orbit coupling (SOC), TaIrTe₄ hosts a minimum of four Weyl points within the first Brillouin zone. Experimental results from quantum oscillations¹⁵ and ARPES^{16,17} measurements were able to identify the Weyl points by comparing the measured electronic structure with the DFT calculations. Interestingly TaIrTe₄ displays a complex electronic structure that can be tuned by external factors like strain which modifies the number of Weyl points or the location of topological nodal lines¹⁸.

In this article, we investigate the topography of the Fermi surface of the Weyl type-II semimetallic candidate NbIrTe₄ via measurements of the de Haas-van Alphen (dHvA) and the Shubnikov-de Haas (SdH) effects to compare with band structure calculations. Similar to T_d -MoTe₂ and WTe₂, NbIrTe₄ is a non-centrosymmetric layered compound belonging to the orthorhombic space group $Pmn2_1$ ¹⁹, as shown in Fig. 1 (a). Based on DFT calculations, eight Weyl points emerge within the first Brillouin zone in the absence of SOC. After including SOC a total of 16 Weyl points emerge between the topmost valence and the lowest conduction band, which makes the electronic structure of NbIrTe₄ more complex than that of its sister compound TaIrTe₄. These nodes are located within 142 meV of the Fermi energy E_F with 8 nodes located in the $k_z = 0$ plane and other 8 in $k_z = \pm 0.2$ planes¹³.

II. METHODS

Single crystals of NbIrTe_4 were grown via a Te flux method. Stoichiometric amounts of elementary Nb (99.999% Alfa Aesar) and Ir (99.99% Sigma Aldrich) with excess Te were heated in a sealed quartz ampule up to 1000°C and then slowly cooled to 700°C . After removing the excess Te via centrifugation the ampules at 700°C , we obtained shiny metallic crystals with dimensions up to $5 \times 1 \times 0.1 \text{ mm}^3$. The inset in Fig. 1(b) shows an image of a typical bar-shaped NbIrTe_4 single-crystal. The crystallographic a -axis is in general aligned along the longest crystal dimension of the crystal and the c -axis along the shortest. The composition and phase purity of our samples was confirmed by energy-dispersive X-ray spectroscopy (EDS) and X-ray diffraction. Initial resistivity and Hall-effect measurements on NbIrTe_4 were performed in a ^4He -cryostat equipped with a 9 T superconducting magnet (Quantum Design PPMS). Experiments under high magnetic fields up to 35 T where performed in resistive Bitter magnets at the National High Magnetic Field Laboratory (NHMFL) in Tallahassee using ^3He cryostats. AC resistivity measurements were performed on single-crystals using the standard 4-wire technique. Additionally, a capacitive cantilever beam technique was used for magnetic torque measurements.

In order to obtain the electronic band structure of NbIrTe_4 and the geometry of its Fermi surface we performed DFT calculations including spin-orbit coupling using the Wien2k package²⁰. The Perdew-Burke-Ernzerhof (PBE) exchange correlation functional²¹ was used in combination with a dense k -mesh of $22 \times 8 \times 8$ k -points and a cutoff RK_{max} of 7.5. The structural parameters were taken from Ref.¹⁹. The angular dependence of the SdH and dHvA frequencies, which are associated to the extremal cross-sectional areas of the Fermi surface through the Onsager relation, the effective cyclotron masses and the charge carrier densities were calculated using the SKEAF code²². For the visualization of the crystal structure and of Fermi surface we used the XCrysden²³ package.

III. RESULTS

The layered structure of NbIrTe_4 is displayed in Fig. 1(a) and it corresponds to a variant of the WTe_2 one as discussed in Ref.¹⁹. Nb and Ir atoms form zigzag chains along the a -direction. When compared to WTe_2 the alternation of Nb and Ir results in a doubling of the unit cell along the b -axis. Measurements of the resistivity ρ in the absence of an external magnetic field reveal metallic behavior with $\rho(T)$ saturating at low temperatures around a residual resistivity $\rho_0 \simeq 16 \mu\Omega\text{cm}$ (see, Fig. 1(b)). The residual resistivity ratio (RRR) which is defined here as $\text{RRR} = \rho(300 \text{ K})/\rho_0$ reaches a value of 17 for this particular sample. However, we consistently found RRR values ranging from 15 to 40 across several

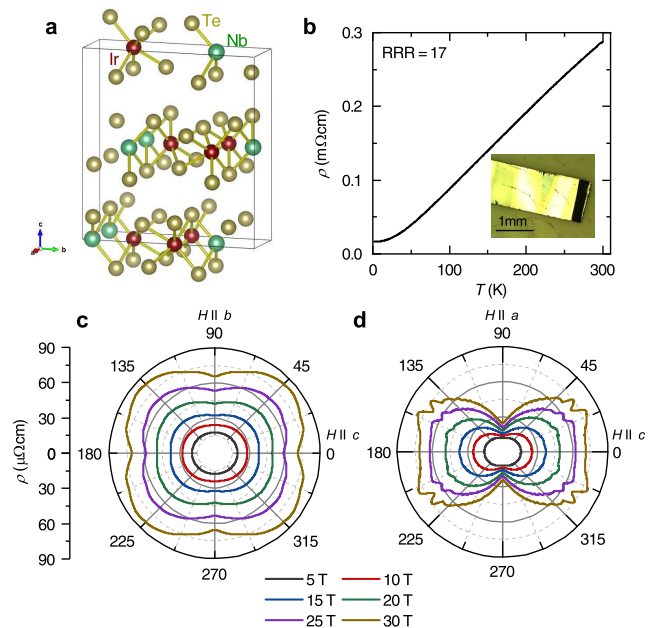


FIG. 1: (a) Crystallographic structure of NbIrTe_4 . Te atoms are depicted as golden spheres while Ir and Nb atoms are represented by red and green spheres, respectively. (b) Resistivity as a function of the temperature for a NbIrTe_4 single-crystal. The inset shows a picture of a typical NbIrTe_4 crystal. (c) and (d) Angular dependence of the resistivity under different magnetic fields at $T = 0.35 \text{ K}$. In (c) the field was rotated within the bc -plane of the crystal with the current $I \parallel a$, 0° corresponds to $\mu_0 H \parallel c$ and 90° to $\mu_0 H \parallel b$. In panel (d) the field was rotated within the ac -plane with $I \parallel b$, 0° is $\mu_0 H \parallel c$ and 90° is $\mu_0 H \parallel a$.

sample batches. Although these RRR values are not particularly high, when compared to other layered transition metal chalcogenides like MoTe_2 , the resulting residual resistivities are relatively low with the presence of quantum oscillations confirming that these crystals are of relative high quality. In this manuscript, we include data from 4 NbIrTe_4 single-crystals used for resistivity and torque measurements at high fields.

The angular dependence of the transverse magnetoresistivity $\rho(\theta)$ of NbIrTe_4 for fields rotating within the ac -plane, and for $I \parallel b$ -axis, is shown in Fig. 1(d). $\rho(\theta)$ is two-fold symmetric with the additional structure emerging at higher fields resulting from the SdH-effect. Its minimum is observed for fields parallel to the a -axis, implying increased inter-layer scattering and a smaller carrier mobility and larger effective masses for fields along this orientation.

For fields rotating in the bc -plane, as in shown in Fig. 1(c), $\rho(\theta)$ displays a significantly smaller anisotropy, when compared to fields rotating in the ac -plane, reaching its maximum for $\theta \approx 45^\circ$ and its minimum for $H \parallel b$. This anisotropy results in a four-fold symmetric ‘‘butterfly’’ shaped angular dependence that is only present

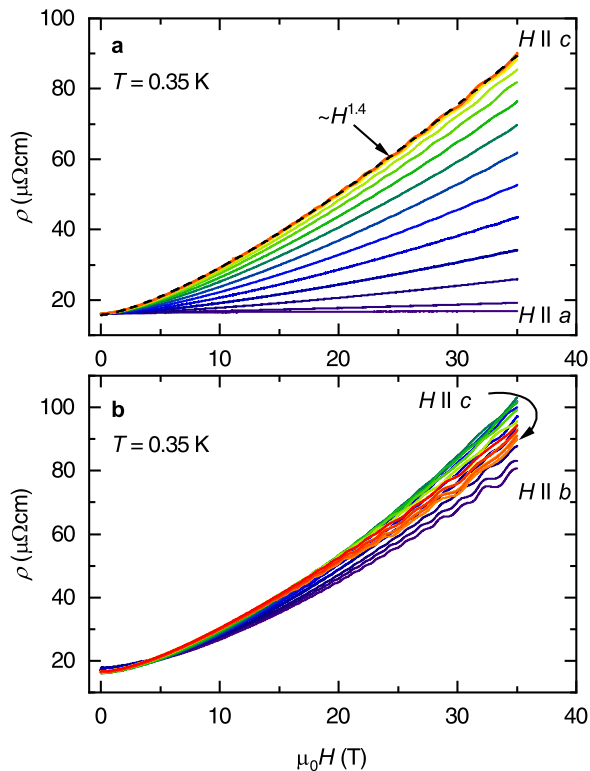


FIG. 2: (a) Resistivity ρ as a function of the magnetic field $\mu_0 H$ for different angles between $\mu_0 H \parallel c$ and $\mu_0 H \parallel a$ -axis. Black dashed line depicts a power law fit of $\rho(\mu_0 H)$ for $\mu_0 H \parallel c$ (red curve). (b) ρ as a function of $\mu_0 H$ for different field orientations in the bc -plane. Above $\mu_0 H \sim 10$ T quantum oscillations superimposed onto the magnetoresistive background are clearly visible in both panels.

under magnetic fields exceeding $\mu_0 H = 10$ T. Under smaller fields the butterfly disappears and $\rho(\theta)$ becomes maximal for $H \parallel c$. This butterfly shaped magnetoresistance was also observed in the high- T_c superconductors²⁴, in magnetic thin films, as well as in the Dirac nodal line semimetal ZrSiS²⁵. In the case of ZrSiS this behavior was ascribed to a topological phase-transition as a function of field orientation that is inherent to the nodal Dirac line²⁵ although the SOC should gap the nodal lines that are located in close proximity to its Fermi level given that they are associated to symmorphism.

Similarly to TaIrTe₄¹⁵, the negative longitudinal magnetoresistance (NLMR) observed in the Weyl type-I monopnictide semimetals^{6,26,27}, which was ascribed to axial anomaly between Weyl points, is absent in NbIrTe₄ for fields and currents along the a -axis. For Weyl type-II semimetals the positive longitudinal magnetoresistance observed in Weyl type-I was originally predicted to depend on the orientation of the external magnetic field relative to wave-vector connecting the Weyl nodes^{8,28}. Although, more recently it was claimed to be orientation independent²⁹. In NbIrTe₄, as well as in

TaIrTe₄, perhaps the Weyl nodes are located too far away from the Fermi level to lead to charge carriers having a well-defined chirality or perhaps that their electrical transport properties are dominated by the topologically trivial bands.

Figure 2 displays the magneto-resistivity $\rho(\mu_0 H)$ as a function of the angle θ for fields rotating within the ac and the bc planes. For $\mu_0 H \parallel c$ -axis SdH oscillations, superimposed onto the magnetoresistive background, become observable when the field exceeds $\mu_0 H \sim 8$ T. But their amplitude weakens as the field is oriented towards the a -direction, limiting the observation of quantum oscillations to $\theta \lesssim 70^\circ$ with respect to the c -axis. For rotations within the bc -plane the SdH oscillations are visible over the entire angular range. Remarkably, over a decade in field the magnetoresistivity can be fit to a single power law where $\rho(\mu_0 H) \propto H^\alpha$ yielding $\alpha = 1.42$. Figure S1 in the Supplementary Information file³⁰ displays the magnetoresistivity in a log-log scale indicating quite clearly the existence of a single, anomalous power law over an extended range of magnetic fields with this exponent being nearly orientation independent. Notice that this value is quite close to the value $\alpha \simeq 1.5$ extracted for TaIrTe₄¹⁵. The first step to address this behavior would be to develop a model within Boltzmann transport theory combining both closed and open orbits, given the geometry of the Fermi surface derived from the calculations which, as shown below, is confirmed by our experiments, including anisotropic effective masses. As discussed by Ref.³¹, such approach is capable of describing non-saturating magnetoresistivity displaying an unconventional power dependence on field in addition to replicating its anisotropy. If conventional transport theory was unable to capture this behavior in a scenario that includes the lack of carrier compensation, one could conjecture that it might bear relation to the existence unconventional quasiparticles.

In order to reveal the topography of the Fermi surface of NbIrTe₄, we performed magneto-resistivity measurements as a function of the angle θ to extract the angular dependence of the SdH frequencies. The results are summarized in Fig. 3, see also Fig. S3 in SI³⁰. To obtain the oscillatory signal, we fit the magnetoresistive background to a polynomial and subsequently subtract it from the experimental curve. The fast Fourier transform of the oscillatory component superimposed onto the resistivity and torque data can be found in the SI material (see, Fig. S3). According to the DFT calculations the Fermi surface of NbIrTe₄ consists of two pairs of spin-orbit split electron (labeled as γ and δ) and hole-pockets (α and β) located near the center of the Brillouin Zone (see, Fig. 3(c)). Three of the four pockets (α , β , and δ) are strongly corrugated cylinders aligned along the k_z and the k_y -directions, respectively. The γ sheet forms an anisotropic “kidney” shaped pocket. As shown in Fig. 6, for magnetic fields oriented along the c -axis we can identify three distinct frequencies F_1 , F_2 and F_3 . Based on their angular dependence F_1 and F_2 can be assigned to the electron pockets and F_3 to the kidney shaped

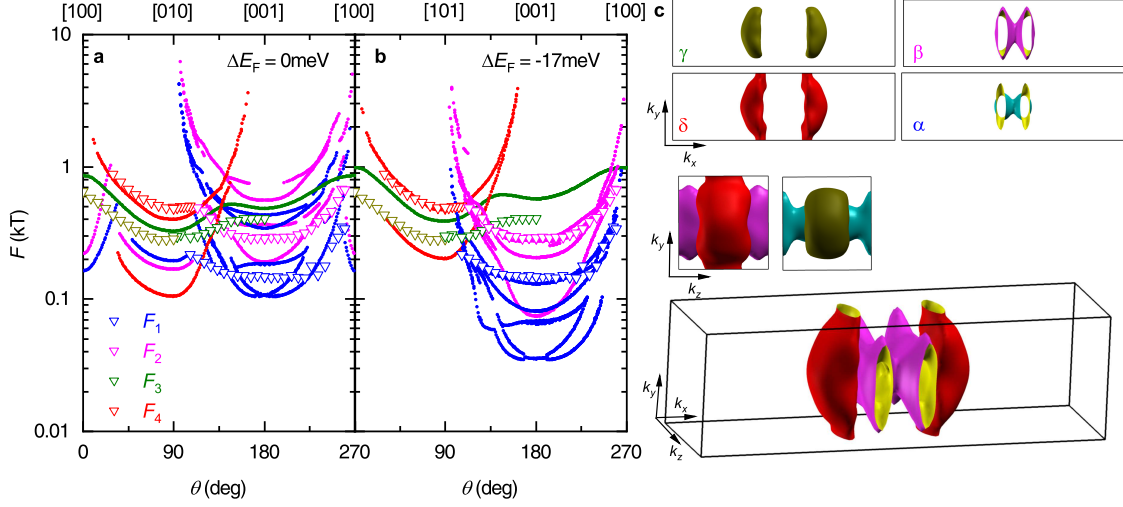


FIG. 3: (a) and (b) Angular dependence of the SdH frequencies $F(\theta)$ for NbIrTe₄. (a) $F(\theta)$ for the position of the Fermi energy E_F resulting from the DFT calculations. (b) $F(\theta)$ with E_F shifted by -17 meV. The smaller solid points represent the SdH frequencies obtained from DFT calculations using the Onsager relation. Larger triangles depict the position of the peaks observed in the Fourier transform of the experimental oscillatory signal superimposed onto the resistivity data. Notice the better agreement between the experimental data and the frequencies resulting from the shift of the Fermi level. F_3 and F_4 can be assigned to the hole pockets labeled as γ and δ in (c), F_1 and F_2 can be assigned to the electron pockets α and β .

hole-pocket. Although the lower calculated frequencies associated to the hole pockets are not clearly visible in the experimental data, we can achieve a quite acceptable agreement between calculated and experimental frequencies by lowering the Fermi level by -17 meV. Only the size of the γ -pocket is overestimated in the calculations by approximately 30%. From the evolution of the Fermi surface with respect to the position of the Fermi energy it is evident that a shift of the γ pocket does not affect the Weyl points in NbIrTe₄ since they appear at touching points between the δ and the β pockets. Since the Weyl type-II points result from band crossings not associated with the band yielding the γ sheet, one can safely state that these nodes are not affected by the accurate position of this band relative to the Fermi level, see band depicted by green line in Fig. S4 within the SI file³⁰.

Further justification for lowering the Fermi level comes from Hall-effect measurements that were performed on a mechanically exfoliated sample with a thickness of $20 \mu\text{m}$ and lateral dimensions of $1\text{-}2 \text{ mm}$. We extract the charge carrier densities and mobilities of NbIrTe₄ from Hall-effect measurements collected between 5 and 100 K under magnetic fields up to 9 T ($\mu_0 H \parallel c$ -axis) by simultaneously fitting the longitudinal magneto-resistivity ρ_{xx} and the Hall resistivity ρ_{xy} to the two-band model:

$$\rho_{xx} = \frac{1}{e} \frac{(n_h \mu_h + n_e \mu_e) + (n_h \mu_e + n_e \mu_h) \mu_h \mu_e B^2}{(n_h \mu_h + n_e \mu_e)^2 + (n_h - n_e)^2 \mu_h^2 \mu_e^2 B^2} \quad (1)$$

$$\rho_{xy} = \frac{B}{e} \frac{(n_h \mu_h^2 - n_e \mu_e^2) + (n_h - n_e) \mu_h^2 \mu_e^2 B^2}{(n_h \mu_h + n_e \mu_e)^2 + (n_h - n_e)^2 \mu_h^2 \mu_e^2 B^2} \quad (2)$$

where n_e , n_h are the electron and hole carrier densities and μ_e , μ_h are the electron and hole carrier mobilities, respectively. In this field interval one obtains a reasonable agreement between the experimental data and the fittings, see Fig. 4(a, b). The mobilities increase as the temperature is lowered to $\mu_e \approx 0.12 \times 10^4 \text{ cm}^2/\text{Vs}$ and $\mu_h \approx 0.1 \times 10^4 \text{ cm}^2/\text{Vs}$ at $T = 5 \text{ K}$, while the electron and the hole densities vary little within this temperature interval. From the low temperature mobilities we can estimate the classical transport lifetime τ_D given by the Drude model, $\tau_D = \mu_{e/h} m^* / e = 3.5 \times 10^{-13} \text{ s}$ with $\mu_{e/h} \approx 0.1 \text{ m}^2/\text{Vs}$ and an effective mass of $m^* = 0.5 m_e$. This result is comparable with the quantum lifetime obtained from SdH oscillations that is related to the Dingle temperature T_D : $\tau_Q = \hbar / 2\pi k_B T_D = 2.3 \times 10^{-13} \text{ s}$. As shown in Fig. 4(d), μ_h is smaller than μ_e for fields parallel to c which can be attributed to larger effective masses for the hole-like orbits when compared to electron ones.

At a temperature of 5 K we obtain $n_e \approx 0.22 \times 10^{20} \text{ cm}^{-3}$ and $n_h \approx 0.48 \times 10^{20} \text{ cm}^{-3}$. Therefore, the density of holes exceeds the density of electrons by a factor greater than 2. In contrast, the volumes of the individual Fermi surface sheets for the unshifted Fermi level (Fig. 5), would yield nearly equal electron and hole

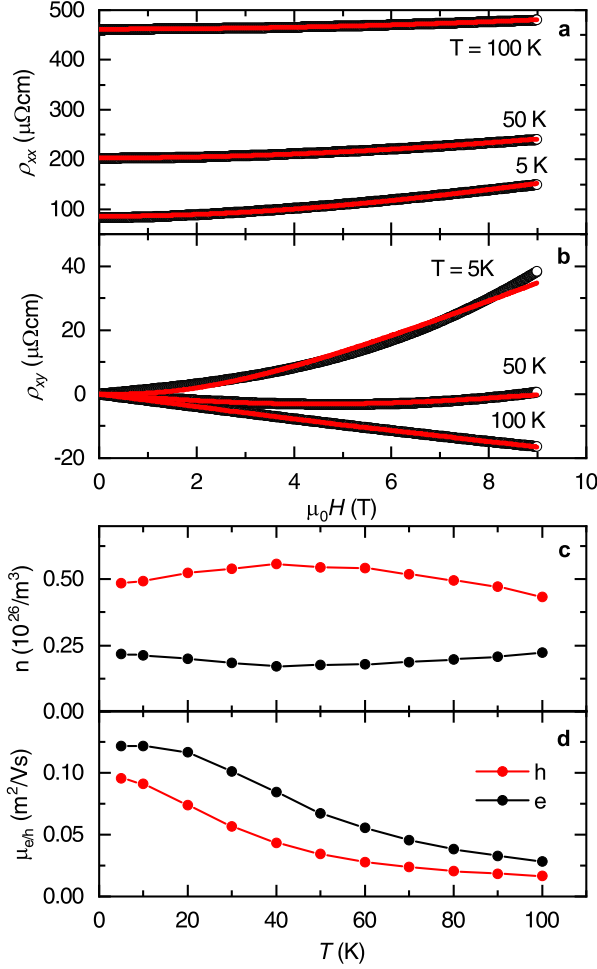


FIG. 4: (a, b) Longitudinal resistivity ρ_{xx} and Hall resistivity ρ_{xy} for NbIrTe₄ as a function of the magnetic field for $T = 5$ K, 50 K and 100 K. The red lines are fits of ρ_{xx} and ρ_{xy} to the two band model (see equation 2). (c, d) Electron and hole carrier densities n_e and n_h , respectively as well as carrier mobilities μ_e and μ_h as a function of the temperature T . Density and mobilities have been extracted from simultaneous fits of the Hall-effect and of the magnetoresistivity data to the two-band model

densities, making NbIrTe₄ a compensated semimetal. As depicted in Fig. 5 lowering the Fermi level leads to an expansion of the volume of the hole pockets while shrinking the electron pockets without fundamentally changing their shape. Thus lowering the Fermi level leads to a reduction in n_e and to an increase in n_h resulting in a better agreement with the Hall-effect data. Hence, NbIrTe₄ is remarkable for not being carrier compensated, and this is consistent with its modest magnetoresistivity, i.e. $\Delta\rho \sim 400\%$ observed at low T s under fields up to $\mu_0 H = 35$ T, while displaying non-saturating magnetoresistivity.

The cyclotron effective mass of a given electronic orbit can be extracted from the temperature damping factor R_T in the Lifshitz-Kosevitch formula and is given

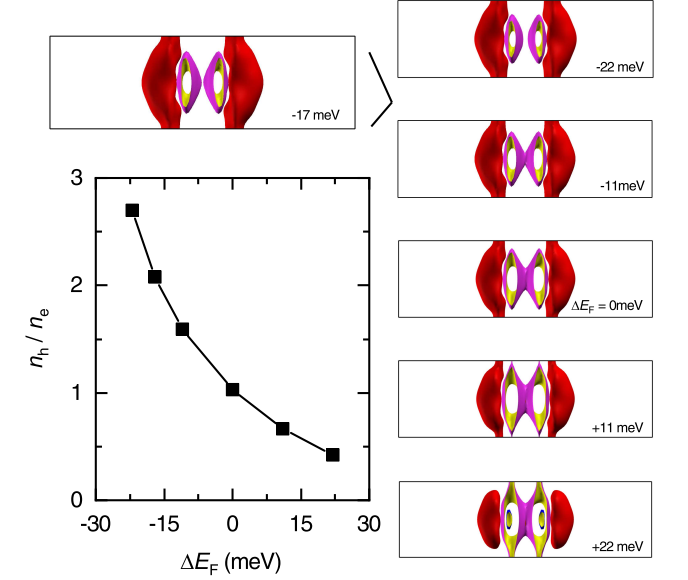


FIG. 5: Fermi surface of NbIrTe₄ projected on the $k_y k_z$ -plane for different displacements ΔE_F of the Fermi level with respect to its original position defined by the DFT calculations. The graph shows the calculated n_h/n_e ratio as a function of ΔE_F .

by: $R_T = \lambda T / \sinh(\lambda T)$ where $\lambda = 2\pi^2 k_B m^* / \hbar e B$, with m^* being the cyclotron effective mass. The fast Fourier transform (FFT) of the oscillatory component superimposed onto the torque data for $\mu_0 H$ nearly parallel to the c -axis is shown in the Fig. 6(a). There are at least three distinct frequencies, which we label as F_1 , F_2 and F_3 . Each correspond to a distinct extremal cross-sectional area of the Fermi surface and belong to different Fermi surface pocket (α , β , γ). To extract m^* for each individual orbit, we fit R_T to the temperature dependence of the amplitude of the peaks observed in the FFT spectra (Fig. 6(b)). As shown in Table I, m^* is anisotropic or depends on sample orientation with respect to $\mu_0 H$ ranging from 0.46 to twice the free electron mass. These values are comparable to those extracted for TaIrTe₄¹⁵.

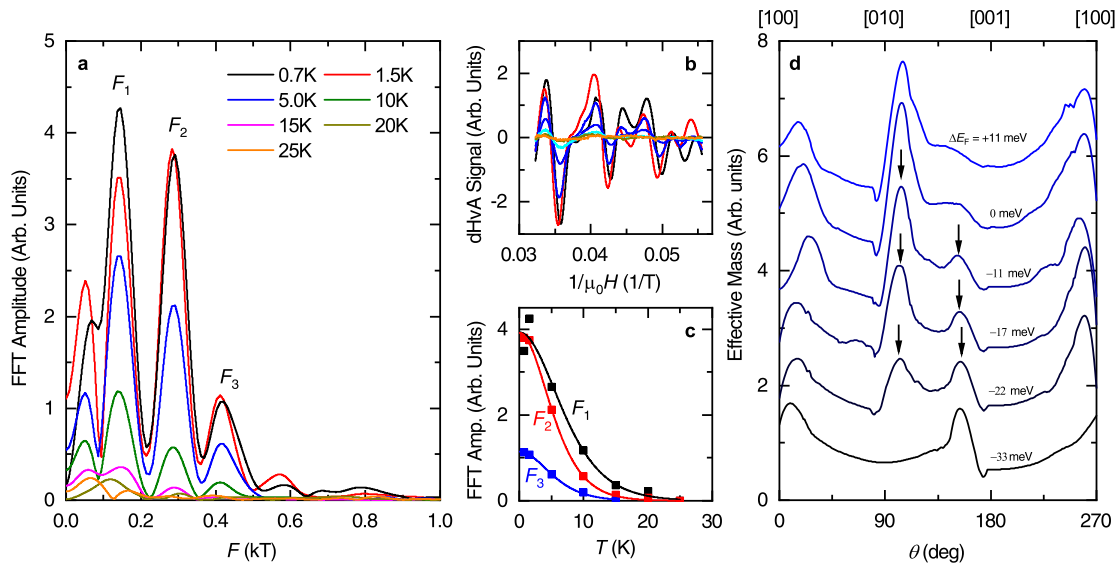


FIG. 6: Effective masses of NbIrTe₄ extracted from quantum oscillations. (a) Fast Fourier Transform (FFT) of the oscillatory component on the torque signal shown in (b) for $H \parallel c$. Frequencies that can be assigned to individual orbits on the Fermi surface pockets are labeled as F_1 , F_2 and F_3 . (b) de Haas-van Alphen oscillations in NbIrTe₄ for temperatures between 0.7 K and $T = 20$ K. (c) FFT amplitude as a function of the temperature for the dHvA frequencies F_1 , F_2 and F_3 . Solid lines represent fits to the temperature damping factor R_T in the Lifshitz-Kosevitch formalism from which we extract the effective masses. (d) Angular dependence of the cyclotron effective mass averaged across all extremal orbits as obtained from the DFT calculations. For the sake of clarity, these curves are shifted with respect to their respective Fermi levels. The curve assigned to $\Delta E_F = 0$ corresponds to the unshifted Fermi energy. Arrows indicate maxima in the average effective mass for fields oriented nearly along the b - or the c -axis. We argue that this anisotropy in effective masses leads to the butterfly shaped magnetoresistivity.

pocket	θ ($^\circ$)	m^* (m_0)	F (kT)
α	135	0.76	0.178
	180 (c)	0.47	0.148
β	180 (c)	0.62	0.289
	225	1.0	0.341
γ	45	0.46	0.372
	90 (b)	1.7	0.299
δ	125	0.55	0.332
	45	2.0	0.729
	90 (b)	1.36	0.496

TABLE I: Effective masses of NbIrTe₄ for selected SdH and dHvA frequencies. The pockets are labeled as α , β , γ and δ following Figs. (3,6). The angle θ represents the orientation of the magnetic field where $\theta = 0^\circ = 270^\circ \equiv \mu_0 H \parallel a$, $90^\circ \equiv \mu_0 H \parallel b$ and $180^\circ \equiv \mu_0 H \parallel c$, where m^* is the cyclotron effective mass in units of the free electron mass m_0 , and F the SdH/dHvA frequency.

As seen in Table I, m^* scales with the size of the extremal cross-sectional orbit with the exception of the γ pocket, which shows an enhanced effective mass for $H \parallel b$. The presence of open orbits for fields aligned along the crystallographic axes, due to the topography of the Fermi surface is likely to affect the angular dependence

of the magnetoresistance and this might explain the butterfly shaped magnetoresistance. As illustrated in Fig. 6(d), the calculated average effective mass is enhanced along high symmetry directions due to the presence of open orbits but depends on the position of the Fermi level. For small shifts ranging from -11 to -22 meV the cyclotron effective shows a maximum along the b - and the c - axes but a minimum in between. This would result in a lower carrier mobility $\mu = q\tau/m^*$ (where q is the charge of the carrier and τ the average scattering time) and hence in a smaller magnetoresistivity for fields along the crystallographic b - and the c -axis, when compared to fields oriented in between both axes which yield closed cyclotron orbits. In addition, for fields along either the c - or the b -axis, the magnetoresistivity results solely from cyclotron orbits on the electron- or on the hole-pockets with open orbits on the hole and electron surfaces, respectively. For fields orientated between both axes, one has cyclotron orbits on both sets of Fermi surfaces thus enhancing the magnetoresistivity with respect to fields along either axis. As for the anisotropy of the magnetoresistivity observed at low fields (see Figs. 1(c) and 1(d)) it results from the larger mobilities extracted for the electron orbits relative to the hole ones.

IV. SUMMARY

In summary, we found that the geometry of the Fermi surface of NbIrTe₄ obtained from the DFT calculations and from quantum oscillation measurements are in rather good agreement, if one considers a small shift in the position of the Fermi energy which does not affect the existence of Weyl type-II nodes. Our overall results support the presence of Weyl points in this material although it displays rather conventional transport properties. Furthermore, our results contrast to our previous studies on *T_d*-MoTe₂³² and WP₂³³, which are also predicted to display a Weyl type-II semimetallic state, but whose experimental Fermi surfaces derived from quantum oscillations can only be captured by DFT after electron and hole bands are independently displaced towards higher and lower energies, respectively. For both compounds this ad-hoc procedure would suppress their Weyl points, in contrast to their robustness in NbIrTe₄. Both quantum oscillations and Hall-effect measurements indicate that NbIrTe₄ is not a compensated semimetal and that the unconventional four-fold anisotropy of its angular magnetoresistivity is governed by the topography of its Fermi

surface and related anisotropy in effective masses. The good agreement between bulk measurements and band structure calculations imply that the electronic properties of NbIrTe₄, and hence its topological character, are well-captured by Density Functional Theory calculations. More importantly, since this compound is exfoliable and predicted by DFT to display a quantum-spin-Hall insulator state in the monolayer limit³⁴, as recently found for WTe₂³⁵, our conclusions convey that it would be important to explore edge conduction and the effect of a gate voltage in heterostructures containing monolayers of NbIrTe₄.

V. ACKNOWLEDGMENTS

This work was supported by DOE-BES through award DE-SC0002613. JYC acknowledge NSF DMR-1700030 for partial support. The NHMFL is supported by NSF through NSF-DMR-1644779 and the State of Florida. V.L.Q. is supported by Ames Lab. The Ames Lab is supported by NSF-DMR-1555163

-
- * Electronic address: schoenemann@magnet.fsu.edu
 † Electronic address: balicas@magnet.fsu.edu
- ¹ B. Yan and C. Felser, *Annu. Rev. Condens. Matter Phys.* **8**, 337 (2017); N. P. Armitage, E. J. Mele, A. Vishwanath, *Rev. Mod. Phys.* **90**, 015001 (2018).
 - ² S.-M. Huang, S.-Y. Xu, I. Belopolski, C.-C. Lee, G. Chang, B. Wang, N. Alidoust, G. Bian, M. Neupane, C. Zhang, S. Jia, A. Bansil, H. Lin, and M. Z. Hasan, *Nat. Commun.* **6**, 7373 (2015).
 - ³ S.-Y. Xu, I. Belopolski, N. Alidoust, M. Neupane, G. Bian, C. Zhang, R. Sankar, G. Chang, Z. Yuan, C.-C. Lee, S.-M. Huang, H. Zheng, J. Ma, D. S. Sanchez, B. Wang, A. Bansil, F. Chou, P. P. Shibayev, H. Lin, S. Jia and M. Z. Hasan, *Science* **349**, 613-617 (2015).
 - ⁴ B. Q. Lv, H. M. Weng, B. B. Fu, X. P. Wang, H. Miao, J. Ma, P. Richard, X. C. Huang, L. X. Zhao, G. F. Chen, Z. Fang, X. Dai, T. Qian, and H. Ding, *Phys. Rev. X* **5**, 031013 (2015).
 - ⁵ H. Weng, C. Fang, Z. Fang, B. A. Bernevig, and X. Dai, *Phys. Rev. X* **5**, 011029 (2015).
 - ⁶ X. Huang, L. Zhao, Y. Long, P. Wang, D. Chen, Z. Yang, H. Liang, M. Xue, H. Weng, Z. Fang, X. Dai, and G. Chen, *Phys. Rev. X* **5**, 031023 (2015).
 - ⁷ P. J. W. Moll, N. L. Nair, T. Helm, A. C. Potter, I. Kimchi, A. Vishwanath, and J. G. Analytis, *Nature* **535**, 266 (2016).
 - ⁸ A. A. Soluyanov, D. Gresch, Z. Wang, Q. Wu, M. Troyer, X. Dai, and B. A. Bernevig, *Nature* **527**, 495 (2015).
 - ⁹ Y. Sun, S.-C. Wu, M. N. Ali, C. Felser, and B. Yan, *Phys. Rev. B* **92**, 161107(R) (2015).
 - ¹⁰ Z. Wang, D. Gresch, A. A. Soluyanov, W. Xie, S. Kushwaha, X. Dai, M. Troyer, R. J. Cava, and B. A. Bernevig, *Phys. Rev. Lett.* **117**, 056805 (2016).
 - ¹¹ G. Autès, D. Gresch, M. Troyer, A. A. Soluyanov, and O. V. Yazyev, *Phys. Rev. Lett.* **117**, 066402 (2016).
 - ¹² K. Koepf, D. Kasinathan, D. V. Efremov, S. Khim, S. Borisenko, B. Büchner, and J. van den Brink, *Phys. Rev. B* **93**, 201101 (2016).
 - ¹³ L. Li, H.-H. Xie, J.-S. Zhao, X.-X. Liu, J.-B. Deng, X.-R. Hu, and X.-M. Tao, *Phys. Rev. B* **96**, 024106 (2017).
 - ¹⁴ J. Liu, H. Wang, C. Fang, L. Fu, and X. Qian, *Nano Lett.* **17**, 467 (2017).
 - ¹⁵ S. Khim, K. Koepf, D. V. Efremov, J. Klotz, T. Förster, J. Wosnitza, M. I. Sturza, S. Wurmehl, C. Hess, J. van den Brink, and B. Büchner, *Phys. Rev. B* **94**, 165145 (2016).
 - ¹⁶ I. Belopolski, P. Yu, D. S. Sanchez, Y. Ishida, T.-R. Chang, S. S. Zhang, S.-Y. Xu, H. Zheng, G. Chang, G. Bian, H.-T. Jeng, T. Kondo, H. Lin, Z. Liu, S. Shin, and M. Z. Hasan, *Nat. Commun.* **8**, 942 (2017).
 - ¹⁷ E. Haubold, K. Koepf, D. Efremov, S. Khim, A. Fedorov, Y. Kushnirenko, J. van den Brink, S. Wurmehl, B. Büchner, T. K. Kim, M. Hoesch, K. Sumida, K. Taguchi, T. Yoshikawa, A. Kimura, T. Okuda, and S. V. Borisenko, *Phys. Rev. B* **95**, 241108(R) (2017).
 - ¹⁸ X. Zhou, Q. Liu, Q. S. Wu, T. Nummy, H. Li, J. Griffith, S. Parham, J. Waugh, E. Emmanouilidou, B. Shen, O. V. Yazyev, N. Ni, and D. Dessau, *Phys. Rev. B* **97**, 241102(R) (2018).
 - ¹⁹ A. Mar, S. Jovic, and J. A. Ibers, *J. Am. Chem. Soc.* **114**, 8963 (1992).
 - ²⁰ P. Blaha, K. Schwarz, P. Sorantin, and S. Trickey, *Comput. Phys. Commun.* **59**, 399 (1990).
 - ²¹ J. P. Perdew, K. Burke, and M. Ernzerhof, *Phys. Rev. Lett.* **77**, 3865 (1996).
 - ²² P. Rourke and S. Julian, *Comput. Phys. Commun.* **183**, 324 (2012).
 - ²³ A. Kokalj, *J. Mol. Graph.* **17**, 176 (1999).

- ²⁴ V. P. Jovanović, L. Fruchter, Z. Z. Li, and H. Raffy, *Phys. Rev. B* **81**, 134520 (2010).
- ²⁵ M. N. Ali, L. M. Schoop, C. Garg, J. M. Lippmann, E. Lara, B. Lotsch, and S. S. P. Parkin, *Sci. Adv.* **2**, 1601742 (2016).
- ²⁶ J. Hu, J. Y. Liu, D. Graf, S. M. A. Radmanesh, D. J. Adams, A. Chuang, Y. Wang, I. Chiorescu, J. Wei, L. Spinu, and Z. Q. Mao, *Sci. Rep. (UK)* **6** (2016).
- ²⁷ F. Arnold, C. Shekhar, S.-C. Wu, Y. Sun, R. D. dos Reis, N. Kumar, M. Naumann, M. O. Ajeesh, M. Schmidt, A. G. Grushin, J. H. Bardarson, M. Baenitz, D. Sokolov, H. Borrmann, M. Nicklas, C. Felser, E. Hassinger, and B. Yan, *Nat. Commun.* **7**, 11615 (2016).
- ²⁸ M. Udagawa, and E. J. Bergholtz, *Phys. Rev. Lett.* **117**, 086401 (2016).
- ²⁹ G. Sharma, P. Goswami, and S. Tewari, *Phys. Rev. B* **96**, 045112 (2017).
- ³⁰ See Supplemental Material at <http://link.aps.org/supplemental/> for a log-log plot of the magnetoresistivity of NbIrTe₄, electronic band structure along specific *k*-directions, Fast Fourier transform of the quantum oscillatory signal as a function of the field orientation, and two-band model fits of the magnetoresistivity and Hall-effect data.
- ³¹ S. N. Zhang, Q. S. Wu, Y. Liu and O. V. Yazyev, *Phys. Rev. B* **99**, 035142 (2019).
- ³² D. Rhodes, R. Schönemann, N. Aryal, Q. Zhou, Q. R. Zhang, E. Kampert, Y.-C. Chiu, Y. Lai, Y. Shimura, G. T. McCandless, J. Y. Chan, D. W. Paley, J. Lee, A. D. Finke, J. P. C. Ruff, S. Das, E. Manousakis, and L. Balicas, *Phys. Rev. B* **96**, 165134 (2017).
- ³³ R. Schönemann, N. Aryal, Q. Zhou, Y.-C. Chiu, K.-W. Chen, T. J. Martin, G. T. McCandless, J. Y. Chan, E. Manousakis, and L. Balicas *Phys. Rev. B* **96**, 121108(R) (2017).
- ³⁴ J. Liu, H. Wang, C. Fang, L. Fu, and X. Qian, *Nano Lett.* **17**, 467 (2017).
- ³⁵ S. Wu, V. Fatemi, Q. D. Gibson, K. Watanabe, T. Taniguchi, R. J. Cava, P. Jarillo-Herrero, *Science* **359**, 76 (2018).